One-dimensional models for supercritical and subcritical transitions in rotating convection

Sutapa Mandal ⬤,[*] Snehashish Sarkar ⬤,[†] and Pinaki Pal ⬤[‡]
Department of Mathematics, National Institute of Technology, Durgapur 713209, India

Numerous studies on natural and man made systems including rotating convection report the phenomena of supercritical and subcritical transitions from one state to another with the variation of relevant control parameters. However, the complexity of the rotating convection system even under the idealized Rayleigh-Bénard geometry hindered the simplest possible description of these transitions to convection. Here we present a one-dimensional description of the stationary subcritical and supercritical transitions to rotating Rayleigh-Bénard convection both for rigid and free-slip boundary conditions. The analysis of the one-dimensional models and performance of three-dimensional direct numerical simulations of the system show qualitatively similar results in a wide region of the parameter space. A brief discussion on time dependent convection of overstable origin is also presented.

I. INTRODUCTION

The phenomenon of transition from one state to the other in a system with the variation of control parameters is ubiquitous [1–3], and is characterized by an order parameter. Examples include transition from conduction to convection [4,5], vapor to liquid [6] and laminar to turbulent [7] in fluids, graphite to diamond [8], ferromagnetic to paramagnetic [9] etc. Depending on the nature of the system, the order parameter may exhibit continuous or discontinuous transitions at a critical value of the parameter. These transitions are connected with the supercritical and subcritical bifurcations of the system, respectively, and are named accordingly.

The current deals with the problem of thermal convection in the presence of rotation. The phenomenon of thermal convection is observed in wide variety of natural as well as man made systems including geophysical [1], astrophysical [3], oceanic [10], liquid metals [11–13], liquid crystal [14,15] etc., and it is one of the key factors governing the dynamics there. The richness of dynamics in such systems in the accessible parameter ranges attracted the attention of researchers for a long time, and kept the field an active area of research [16–23]. To unfold the complexity of thermal convection, researchers often rely on the plane layer Rayleigh-Bénard convection (RBC) model for the investigation of convective phenomena like instabilities [16,24–27], patterns [28–30], chaos [31–33], heat transfer [7,12,34,35], turbulence [5,36] etc. For a fixed investigation domain, RBC is completely described by two parameters, namely, the Rayleigh number (Ra, measures the vigor of the buoyancy force) and the Prandtl number (Pr, ratio of the thermal and viscous diffusion time scales).

---

[*]Present address: School for Engineering of Matter, Transport and Energy, Arizona State University, Tempe, AZ 85287, USA; Contact author: sutapamandal530@gmail.com

[†]Contact author: snehashishsarkar23@gmail.com

[‡]Contact author: ppal.maths@nitdgp.ac.in

The study of RBC for more than a century [4,7,16,37] has not only improved the understanding of thermal convection but also contributed significantly in developing subjects like hydrodynamic and hydromagnetic instabilities [4], pattern formation [29,30], and nonlinear dynamics [38]. However, for geophysical [39], oceanic [10] and astrophysical [40,41] systems where convection occurs in the presence of rotation, rotating Rayleigh-Bénard convection (RRBC) provide a better model. The presence of rotation introduces centrifugal as well as Coriolis forces into the system along with the buoyancy force and makes the problem more complex compared to its nonrotating counterpart [4,37,42].

In this paper, we consider RRBC of low Prandtl number fluids, the description of which needs one more dimensionless parameter, namely, the Taylor number (Ta, measures the strength of the rotation about a vertical axis) along with Ra and Pr. Chandrasekhar [4] developed the linear theory based on normal mode analysis to determine the critical Rayleigh number (Ra_c) and wave number (k_c) for the onset of RRBC both in the presence of free-slip and no-slip velocity boundary conditions. Linear theory results show that the rotational constraint inhibits convection by pushing the critical Rayleigh number for the onset of stationary as well as oscillatory convection toward higher Ra which is also experimentally supported [43,44]. It is interesting to note here that in the presence of free slip boundaries, for higher Ta and Pr < 0.677, the time dependent overstable solutions are observed at the onset because they can reduce the stabilizing effect of rotation [4,45]. Thus, in this case, the oscillatory convection occurs at a much lower critical Rayleigh number compared to the one required for stationary convection and hence, convective motion of overstable origin is preferred there. Beyond the onset of convection, RRBC has been extensively investigated theoretically [45–48], numerically [49–53] and experimentally [42,54–57]. These studies revealed several interesting properties of rotating convection related to instabilities, bifurcations, pattern dynamics, and turbulence.

However, here we focus on the primary instability and the related flow patterns near the onset of convection. Of particular interest is the subcritical convection leading to a finite amplitude solution at the onset. The existence of such subcritical convection was first theoretically shown in RRBC with free slip boundary conditions using perturbation methods [45] and low dimensional modeling [58]. On the other hand, the first experimental observation of subcritical rotating convection was reported by Rossby [42]. Subsequently, Clever and Busse [59] numerically examined subcritical convection in low Prandtl number fluids in the presence of rigid boundaries. The theoretical analysis of Clune and Knobloch [47] based on weakly nonlinear theory, followed by the simultaneous experimental and numerical study of Bajaj *et al.* [56] also provided great insight into the phenomenon of subcritical convection and associated finite amplitude solution at the onset of RRBC.

Recently, in extensive three-dimensional direct numerical simulations with rigid boundaries, Mandal *et al.* [22] identified the region of the parameter space for the observation of finite amplitude solution at the onset of convection. Along with the direct numerical simulations, a low dimensional model (22-dimensional) is also used to analyze the finite amplitude solutions at the onset, and the origin of it is connected to the subcritical pitchfork bifurcation of the basic conduction state. The investigation also revealed that the subcriticality is promoted with increasing Ta while it is inhibited with increasing Pr in the stationary convection regime. However, a simplified description of the phenomenon is still missing, due to the inherent complexity of the RRBC system.

Here we revisit the problem of subcritical rotating convection in low Prandtl number fluids with the objective of providing the simplest possible description of the phenomena. The study is performed using the RRBC model with both rigid and free-slip boundary conditions by varying the Prandtl number in the range $0 < Pr \leqslant 0.6$. For rigid boundaries, the Taylor number is varied in the range $0 < Ta \leqslant 5 \times 10^4$ and for free-slip boundaries, it is varied in the range $0 < Ta \leqslant 10^4$. Two one-dimensional models, one each for rigid and free-slip boundary conditions are derived using Galerkin projection and adiabatic elimination process for that purpose, which nicely captures the phenomena of subcritical convection and related transitions. We also perform direct numerical simulations (DNS) of the system in said parameter regime. The model and DNS results show a qualitative match. Additionally, we also investigate the onset of overstable convection in this paper.

II. PROBLEM FORMULATION

A. Physical system and governing equations

Standard plane layer Rayleigh-Bénard convection systems consisting of a thin horizontal layer of Newtonian fluid of thickness d, kinematic viscosity ν, thermal diffusivity κ and coefficient of volume expansion α confined between two perfectly thermally conducting horizontal plates are considered for the study. The convective motion is driven by the buoyancy force generated due to the thermal gradient between the upper and lower plates, maintained at constant temperatures T_u and T_l, respectively, with $\Delta T = T_l - T_u > 0$. The system is rotated about the vertical axis with an angular velocity $\boldsymbol{\Omega}$ ($=\Omega\hat{\mathbf{e}}_z$, $\hat{\mathbf{e}}_z$ being the vertically upward unit vector). As ΔT crosses a critical value for fixed other parameters, the convective motion of the fluid in the presence of rotation is described by the following set of dimensionless Boussinesq-Oberbeck [60,61] equations with respect to a frame of reference corotating with the system:

$$\frac{\mathcal{D}\mathbf{u}}{\mathcal{D}t} = -\boldsymbol{\nabla}\pi + \nabla^2\mathbf{u} + \mathrm{Ra}\theta\hat{\mathbf{e}}_z + \sqrt{\mathrm{Ta}}(\mathbf{u} \times \hat{\mathbf{e}}_z), \tag{1a}$$

$$\frac{\mathcal{D}\theta}{\mathcal{D}t} = \frac{1}{\mathrm{Pr}}[u_z + \nabla^2\theta], \tag{1b}$$

$$\boldsymbol{\nabla} \cdot \mathbf{u} = 0, \tag{1c}$$

where $\frac{\mathcal{D}}{\mathcal{D}t} \equiv \frac{\partial}{\partial t} + (\mathbf{u} \cdot \boldsymbol{\nabla})$ represents the material derivative, and $\mathbf{u}(x, y, z, t) = (u_x, u_y, u_z)$, $\theta(x, y, z, t)$, and $\pi(x, y, z, t)$ are the convective velocity, temperature, and pressure fields, respectively. Note that the convective pressure field $\pi(x, y, z, t)$ includes the contribution of the centrifugal acceleration. The scales d, d^2/ν, and $\Delta T\nu/\kappa$ for length, time, and temperature, respectively, are used to make Eqs. (1a)–(1c) dimensionless. The Rayleigh and Prandtl numbers are defined by $\mathrm{Ra} = \alpha g\Delta T d^3/(\nu\kappa)$ and $\mathrm{Pr} = \nu/\kappa$, where g is the acceleration due to gravity. Another parameter called the reduced Rayleigh number (r) is used subsequently and it is defined by $\mathrm{r} = \mathrm{Ra}/\mathrm{Ra}_c$, where Ra_c is the critical Rayleigh number for the onset of convection.

B. Boundary conditions

In this paper, we have used both rigid and free-slip velocity boundary conditions. The horizontal plates are assumed to be thermally conducting. For rigid and free-slip boundaries, the origin of the coordinate axes is taken at the mid plane and the bottom plate, respectively. The positive z axis is taken antiparallel to the gravity.

Therefore, for rigid and thermally conducting boundaries we have

$$u_x = u_y = u_z = \theta = 0 \quad \text{at} \quad z = \pm\tfrac{1}{2}, \tag{2}$$

while free-slip conducting boundaries imply

$$u_z = \frac{\partial u_x}{\partial z} = \frac{\partial u_y}{\partial z} = \theta = 0 \quad \text{at} \quad z = 0, 1. \tag{3}$$

Thus, Eqs. (1a)–(1c) together with the relevant boundary conditions provide the mathematical model of the rotating hydrodynamic system.

III. LINEAR THEORY

To determine the onset of convection, the linear stability analysis of the conduction state of the system is performed both with rigid and free-slip boundary conditions. First, the convective fields

are expanded in terms of the normal modes as

$$
\begin{bmatrix} \mathbf{u} \\ \theta \\ \pi \end{bmatrix} = \begin{bmatrix} \mathbf{U}(z) \\ \Theta(z) \\ \Pi(z) \end{bmatrix} e^{i(k_x x + k_y y) + \sigma t} + \text{c.c.}, \tag{4}
$$

where c.c., $\mathbf{U}(z) = (\mathrm{U}_x(z), \mathrm{U}_y(z), \mathrm{U}_z(z))$, k_x, and k_y stand for the complex conjugate, z dependent factor of the velocity vector, and the components of the wave vector in the x and y directions, respectively. The temporal growth rate of perturbations is represented by $\sigma = \sigma_r + i\sigma_i$. Substituting the above normal modes in the governing equations (1a)–(1c) and retaining the linear terms, the following set of equations are obtained:

$$(D^2 - k^2 - \sigma)\mathbf{U}(z) + \sqrt{\mathrm{Ta}}(\mathbf{U}(z) \times \hat{\mathbf{e}}_3) = ik_x \Pi(z)\hat{\mathbf{e}}_1 + ik_y \Pi(z)\hat{\mathbf{e}}_2 + (D\Pi(z) - \mathrm{Ra}\Theta(z))\hat{\mathbf{e}}_3, \tag{5a}$$

$$(D^2 - k^2 - \sigma \mathrm{Pr})\Theta(z) + \mathrm{U}_z(z) = 0, \tag{5b}$$

$$ik_x \mathrm{U}_x(z) + ik_y \mathrm{U}_y(z) + D\mathrm{U}_z(z) = 0, \tag{5c}$$

where $D \equiv \frac{d}{dz}$ and $k = \sqrt{k_x^2 + k_y^2}$ is the horizontal wave number. These equations along with the considered boundary conditions are then discretized using a staggered-grid Chebyshev spectral collocation method [62] along the vertical direction as outlined in [22] which leads to a generalized eigenvalue problem given by

$$\mathrm{AX} = \sigma \mathrm{BX}, \tag{6}$$

where, A and B are square matrices each of dimension $5N + 4$, N is the order of the Chebyshev polynomial, and σ is the eigenvalue. Note that the matrices A and B are functions of the parameters of the system and the spatial grid points given by

$$\phi_l = \cos\left[\frac{\pi l}{N}\right](l = 0, 1, \ldots, N), \quad \phi_{m+\frac{1}{2}} = \cos\left[\left(m + \frac{1}{2}\right)\frac{\pi}{N}\right](m = 0, 1, \ldots, N - 1). \tag{7}$$

The vector X is defined by

$$X = \left(\{\mathrm{U}_x(\phi_l)\}_{l=0}^N, \{\mathrm{U}_y(\phi_l)\}_{l=0}^N, \{\mathrm{U}_z(\phi_l)\}_{l=0}^N, \{\Theta(\phi_l)\}_{l=0}^N, \left\{\Pi(\phi_{m+\frac{1}{2}})\right\}_{m=0}^{N-1}\right)^T.$$

Afterward, we proceed to solve the generalized eigenvalue problem utilizing the QZ algorithm [63]. The trivial conduction state becomes unstable when the real part of one of the eigenvalues becomes positive from negative with the variation of a relevant parameter. One obtains the case of stationary cellular convection, where the so called "principle of the exchange of stabilities" [4] is valid when a real eigenvalue of the problem becomes positive. On the other hand, the case of over-stability is obtained when the real parts of a pair of complex conjugate eigenvalues become positive. Figure 1 shows the typical eigenspectrum of the generalized eigenvalue problem for rigid boundary conditions for two specific sets of parameter values. We then solve the generalized eigenvalue problem in the entire region of the parameter space considered in this paper to determine the critical Rayleigh number Ra_c and the critical wave number k_c for the onset of convection. The critical wave numbers determined from the linear theory are subsequently used for low dimensional modeling and performing direct numerical simulations to define the computational domain. Figures 2(a) and (b) show the regions of stationary and overstable convection regimes on the $\mathrm{Pr} - \mathrm{Ta}$ plane for rigid and free-slip boundary conditions, respectively, determined from the linear theory.

IV. NONLINEAR ANALYSIS

Linear theory only determines the marginally stable state of the system, but it can not determine the flow patterns at the onset which is purely a nonlinear phenomenon. Thus, to investigate the flow patterns at the onset of convection we perform nonlinear analysis of the system. For the nonlinear analysis, we employ a low dimensional modeling technique and simultaneously perform direct numerical simulations of the system both for rigid and free-slip boundary conditions. The results are discussed below.
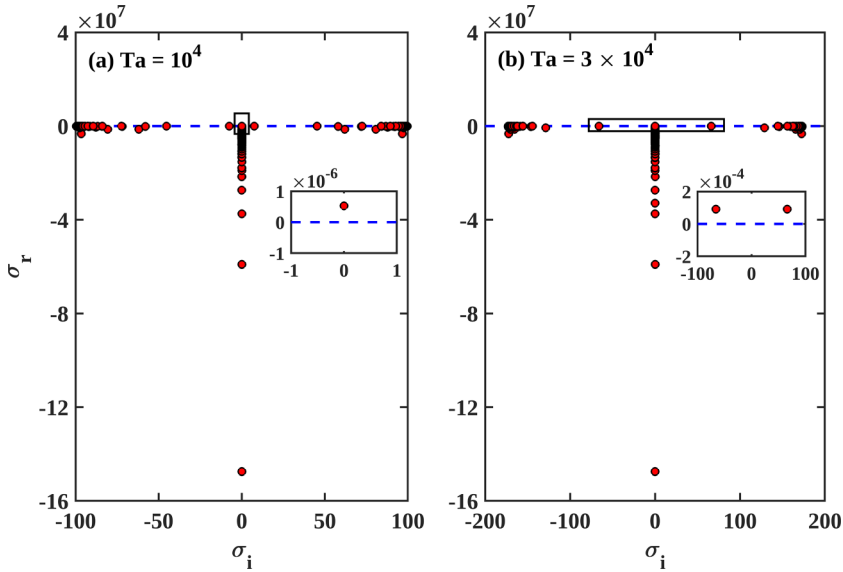
FIG. 1. Full eigenspectrum of the generalized eigenvalue problem (6) with $Pr = 0.1$ in the presence of rigid boundary conditions just above the onset of convection for (a) stationary cellular convection and (b) overstable oscillatory convection.

A. Stationary cellular convection

The primary objective of the paper is to investigate the onset of rotating stationary cellular convection and the related finite amplitude solution, where the principle of the exchange of stabilities is valid. Subsequently, detailed results obtained for rigid and free-slip boundary conditions with $k = k_c$ are presented.
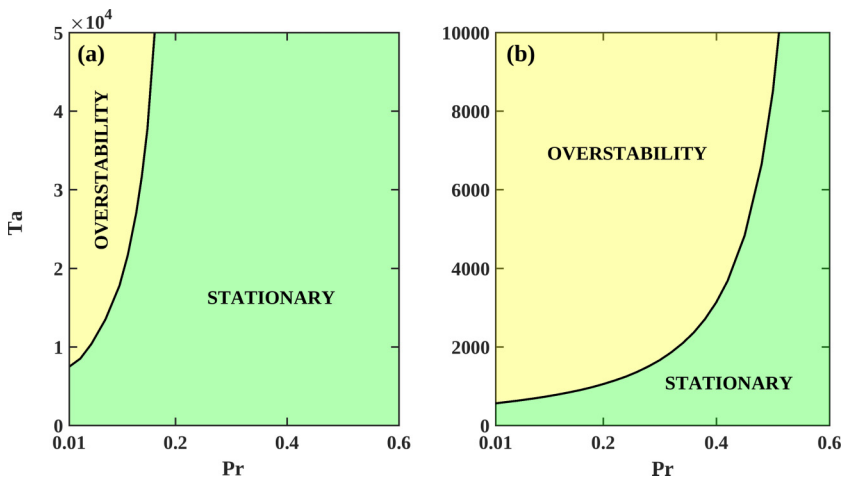

FIG. 2. Stationary and overstable flow regimes at the onset of convection on the $Pr - Ta$ plane for rigid (a) and free-slip (b) boundary conditions.

1. Results for rigid boundary conditions

Here we consider rigid velocity boundary conditions for the analysis of finite amplitude two-dimensional rolls solution of subcritical origin at the onset of convection. First, we perform low dimensional modeling of the system followed by the direct numerical simulations. A minimal mode low dimensional model is constructed by considering the following truncated expansions

$$u_z(x, y, z, t) = W_{101}(t)\cos(k_c x)C_1(\lambda_1 z), \tag{8}$$

$$\omega_z(x, y, z, t) = Z_{201}(t)\cos(2k_c x)\cos(\pi z) + Z_{102}(t)\cos(k_c x)\sin(2\pi z), \tag{9}$$

$$\theta(x, y, z, t) = T_{101}(t)\cos(k_c x)\cos(\pi z) + T_{002}(t)\sin(2\pi z), \tag{10}$$

of vertical velocity u_z, vertical vorticity ω_z, and temperature θ, respectively, in terms of the Chandrasekhar function [4] $C_1(\lambda_1 z) = \frac{\cosh \lambda_1 z}{\cosh \lambda_1/2} - \frac{\cos \lambda_1 z}{\cos \lambda_1/2}$ with $\lambda_1 = 4.73$, sin and cos functions compatible with the boundary conditions. The experimental [42] and numerical [22,59] observation of two-dimensional rolls solutions at the onset of rotating convection, leads to the natural choice of the perturbations $W_{101}(t)\cos(k_c x)C_1(\lambda_1 z)$ in u_z, $\omega_z = 0$ and $T_{101}(t)\cos(k_c x)\cos(\pi z)$ with respect to which the system is marginally stable at the critical Rayleigh number. Next, for the saturation of the marginally stable mode of convection in the simplest possible way, we consider modes $T_{002}(t)\sin(2\pi z)$ in the temperature, and $Z_{201}(t)\cos(2k_c x)\cos(\pi z)$ and $Z_{102}(t)\cos(k_c x)\sin(2\pi z)$ in vertical vorticity.

Now projecting the governing hydrodynamics equations on these five modes, the following set of coupled nonlinear ordinary differential equations is obtained:

$$\dot{\xi} = (a_{11}\xi + a_{12}\zeta + a_{13}\phi)/a_{14}, \tag{11}$$

$$\dot{\zeta} = a_{21}\zeta + a_{22}\xi + a_{23}\eta\xi, \tag{12}$$

$$\dot{\eta} = -a_{31}\eta + a_{32}\zeta\xi, \tag{13}$$

$$\dot{\phi} = (a_{41}\phi + a_{42}\xi + a_{43}\psi\xi)/\text{Pr}, \tag{14}$$

$$\dot{\psi} = (-a_{51}\psi + a_{52}\xi\phi)/\text{Pr}, \tag{15}$$

where $\xi = W_{101}$, $\zeta = Z_{102}$, $\eta = Z_{201}$, $\phi = T_{101}$ and $\psi = T_{002}$, $a_{11} = -(19.74k_c^4 + 9880.87 + 485.70k_c^2)$, $a_{12} = 48.75\sqrt{\text{Ta}}$, $a_{13} = 13.76\text{Ra}k_c^2$, $a_{14} = 19.74(k_c^2 + 12.30)$, $a_{21} = -(39.47 + k_c^2)$, $a_{22} = -4.93\sqrt{\text{Ta}}$, $a_{23} = 2.09$, $a_{31} = 9.86 + 4k_c^2$, $a_{32} = -8.36$, $a_{41} = -(0.99k_c^2 + 9.86)$, $a_{42} = 1.39$, $a_{43} = -5.09\text{Pr}$, $a_{51} = 39.47$, and $a_{52} = 2.54\text{Pr}$.

For the validation of the above model, we first determine the onset of stationary convection from the model (11)–(15) and compare with the linear theory results. The comparisons are shown in Table I. From the table, it is clear that there is a satisfactory match between the linear theory and the model results for the onset of convection. Next we move ahead to reduce the model further to achieve the simplest possible description of the system for the onset of convection in the stationary regime using adiabatic elimination process [64].

To investigate the dynamics of the dynamical system (11) - (15) beyond the onset of convection, we first focus on the stationary convection regime and for that, we need to determine the fixed points of it in the parameter regime of our interest. Thus, we obtain a set of 5 algebraic equations in ξ, ζ, η, ϕ and ψ by equating the right hand sides of the equations (11)–(15). Next, from those 5 equations we eliminate the variables ζ, η, ϕ and ψ, and obtain the following equation in ξ:

$$c_1\xi + c_3\xi^3 + c_5\xi^5 = 0, \tag{16}$$

where $c_5 = a_{23}a_{11}a_{32}a_{43}a_{52}$, $c_3 = a_{11}(a_{21}a_{31}a_{43}a_{52} + a_{23}a_{32}a_{41}a_{51}) - (a_{12}a_{31}a_{22}a_{43}a_{52} + a_{13}a_{42}a_{51}a_{23}a_{32})$, and $c_1 = a_{51}a_{31}[a_{11}a_{41}a_{21} - (a_{12}a_{22}a_{41} + a_{13}a_{42}a_{21})]$.

TABLE I. Critical Rayleigh numbers (Ra_c) for different Ta, computed from the linear theory (LT), 1D model, and DNS for $Pr = 0.1$ with rigid boundary conditions.

Ta	k_c (LT)	Ra_c (LT)	Ra_c (Model)	Ra_c (DNS)	Error(%) (LT vs Model)	Error(%) (LT vs DNS)
1×10	3.119	1720	1734	1715	0.81	0.29
1×10^2	3.159	1764	1779	1760	0.85	0.23
5×10^2	3.317	1948	1976	1940	1.43	0.41
1×10^3	3.482	2159	2205	2150	2.13	0.42
5×10^3	4.263	3476	3706	3380	6.61	2.76

Now using Eq. (16) we construct the following potential function [38,65] for ξ:

$$V(\xi) = - \int (c_1\xi + c_3\xi^3 + c_5\xi^5)d\xi. \tag{17}$$

Note that, although the potential function $V(\xi)$ defined in Eq. (17) contains the variable ξ only, the contributions of the other variables are embedded there in the coefficients. Subsequently, it can be seen that $V(\xi)$ nicely captures the phenomenon of transition to subcritical convection. Now using the potential function $V(\xi)$ we obtain the following one-dimensional dynamical system

$$\dot{\xi} = -\frac{dV(\xi)}{d\xi} = c_1\xi + c_3\xi^3 + c_5\xi^5, \tag{18}$$

which is subsequently used to investigate the onset of subcritical and supercritical rotating convection. Interestingly, the one-dimensional dynamical system (18) captures the dynamics of the five model [(11)–(15)] in the stationary convection regime very closely. The onset of stationary convection determined from the 1D model is the same as the ones presented in Table I. We now perform a detailed bifurcation analysis of the model (18) using an open source software XPPAUT [66] to understand the transition to convection for different values of the parameters.

Figure 3 shows the bifurcation diagrams constructed from the 1D model for fixed $Pr = 0.1$ and various values of Ta. In the bifurcation diagrams, for each value of Ta, the variation of r is shown along the horizontal axis and that of the stable (solid lines) and unstable (dashed lines) fixed points along the vertical axis. The bifurcation diagrams show the transition to convection through supercritical and subcritical pitchfork bifurcations for slow and high rotation rates, respectively. Note that the subcritical transition to convection is characterized by the appearance of a saddle-node (SN) bifurcation at higher Ta, resulting in a discontinuity in the solutions followed by finite amplitude flow patterns at the onset. It is also observed that as the rotation rate is increased, the saddle-node (SN) bifurcation point moves toward lower r, and the distance between the pitchfork bifurcation (PB) and SN points increases. For more details, we look at the variation of the location of the SN bifurcation point with Ta for $Pr = 0.025$ and 0.1 and the results are presented in Fig. 4. From the above discussion, it is apparent that for a fixed value of Pr, increasing rotation leads to an increase in subcriticality. The time series of ξ and the fluid pattern associated with the stable stationary solutions of supercritical origin is shown in Fig. 5. The flow patterns at the onset of subcritical convection are also similar but the associated mean velocity is higher.

To illustrate the transitions from supercritical to the subcritical onset of convection with the variation of rotation rate (Ta) in more detail, we consider two values of Ta, namely, 10 and 500 where, respectively, supercritical and subcritical transition to convection is observed in direct numerical simulations [22,59] with $Pr = 0.1$. For Ta = 10, we first draw the graphs of the potential function $V(\xi)$ by varying the reduced Rayleigh number r around $r = 1$, the critical Rayleigh number for the onset of convection. The graphs are shown in Fig. 6(a).

From Fig. 6(a), only single well potentials are observed for $0 < r \leqslant 1$. The shape of the graphs suggests that $\xi = 0$ is the only fixed point of the system and it is stable, which physically indicates
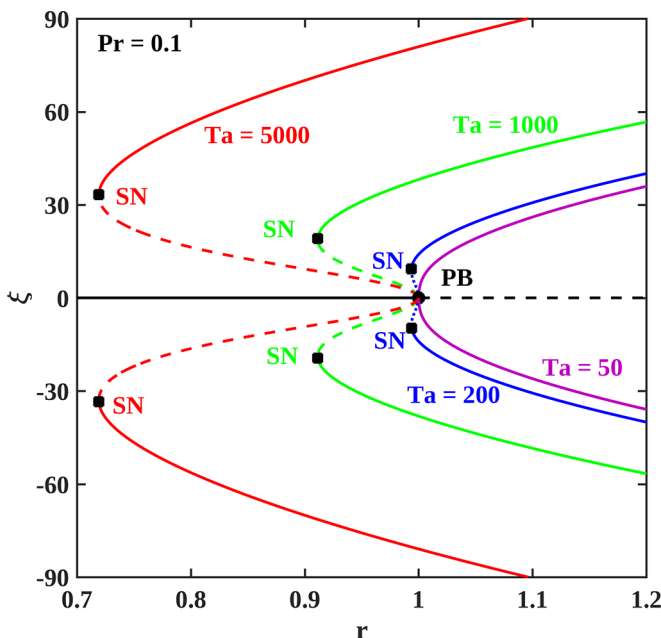
FIG. 3. Bifurcation diagrams prepared from the 1D model for fixed Pr = 0.1 and four different Ta. Pitchfork and saddle-node bifurcation points are marked with PB and SN, respectively. Supercritical pitchfork bifurcation is seen for Ta = 50, while, subcritical pitchfork bifurcations are observed for other three Ta (200, 1000, and 5000).

the stability of the conduction state of the system. On the other hand, for $r > 1$, the shape of the graphs changes and double well potentials are observed. Now, there are three different fixed points (extrema) of the system, namely, the trivial $\xi = 0$ and two other nonzero fixed points (say $\pm\xi^*$) which are marked with black squares in Fig. 6(a). The shape of the graphs indicates that the trivial fixed point is unstable (maxima) and the nonzero fixed points are stable (minima). Note that the stable nonzero fixed points physically represent the stationary two-dimensional roll patterns. Such a scenario is typically observed around a supercritical pitchfork bifurcation [38]. The bifurcation diagram of the one-dimensional model (18) for the same set of parameter values is shown in Fig. 6(b) and confirms the supercritical nature of the transition to convection.
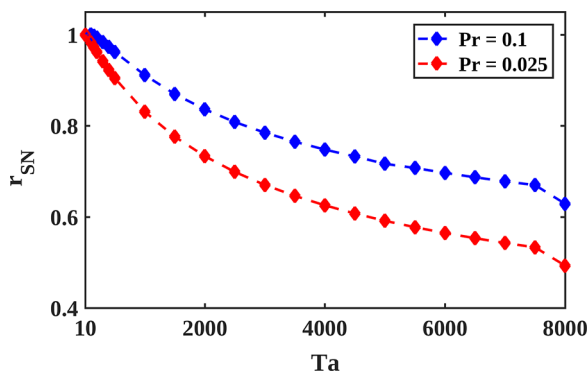

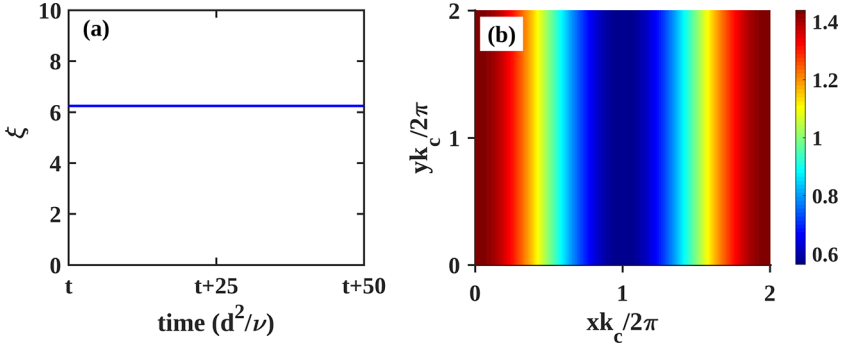FIG. 4. Variation of the saddle node bifurcation point with Ta for two different Pr.

FIG. 5. Time series (a) and corresponding flow pattern (b) at the onset of convection for Ta $= 50$ and Pr $= 0.1$.

Next, for Pr $= 0.1$ and Ta $= 500$, we also draw the graphs of $V(\xi)$ by varying r around the critical value $r = 1$ [Fig. 7(a)]. The fixed points of the system can be identified from the location of the local maxima or minima points of the graph marked by filled black circles, and red and black squares, respectively. The local maxima and minima, respectively, represent unstable and stable fixed points of the system. In this case, only the trivial fixed point ($\xi = 0$) exists and is stable [the filled black circle in Fig. 7(a)] for $0 < r < 0.9616$. Interestingly, five different fixed points (three stable and two unstable) exist in the range $0.9616 < r < 1$. The stable fixed points (filled black circles and squares) are separated by the unstable fixed points (red squares). As a result, the phenomenon of hysteresis is observed in this range of r. Further, increase of r beyond $r = 1$, two unstable nonzero fixed points ceased to exist and only three fixed points exist. The trivial fixed point becomes unstable and finite amplitude stable nonzero fixed points continue to exist. Thus, at the onset of convection, finite amplitude two-dimensional steady flow patterns are observed just at the onset of convection ($r > 1$). This is a signature of subcritical pitchfork bifurcation with hysteresis [38] and related transition to finite amplitude convection is subcritical in nature for the considered set of parameter values. Finally, we use the one-dimensional model once again to construct a bifurcation diagram for the parameter values Pr $= 0.1$ and Ta $= 500$. The bifurcation diagram is shown in Fig. 7(b). The bifurcation clearly shows the scenario of subcritical pitchfork bifurcation with hysteresis around the critical point $r = 1$.
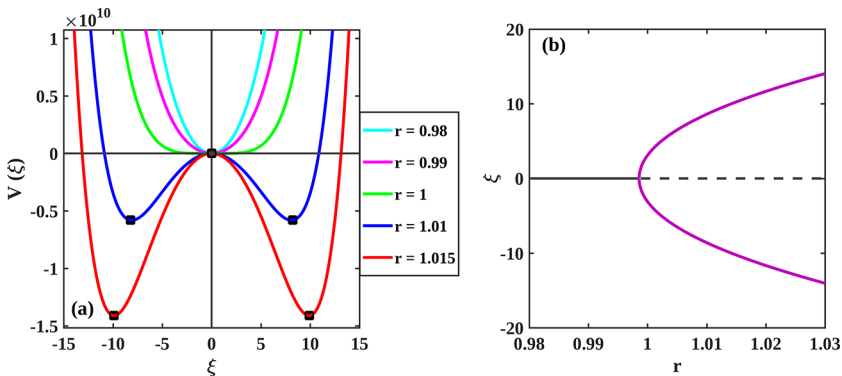

FIG. 6. Supercritical transition to convection for Pr $= 0.1$ and Ta $= 10$. (a) Graphs of $V(\xi)$ for different values of r around the critical point $r = 1$. The extremum points are shown with black squares. (b) Bifurcation diagram of the 1D model (18) showing supercritical pitchfork bifurcation.
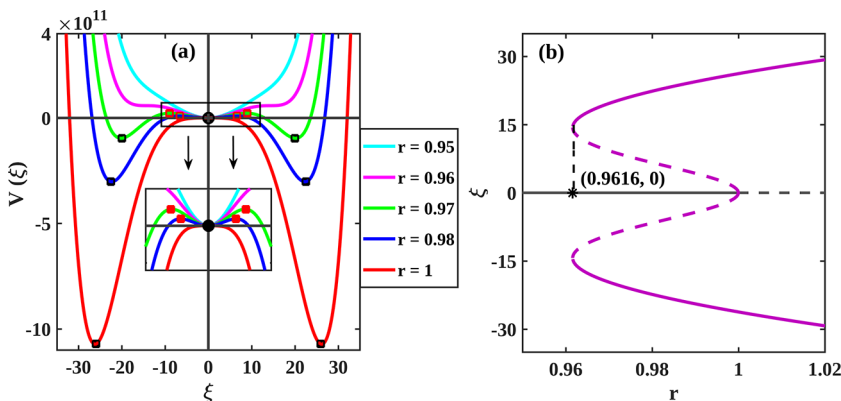
FIG. 7. Subcritical transition to convection for Pr = 0.1 and Ta = 500. (a) Graphs of $V(\xi)$ for different values of r around the critical point $r = 1$. The filled black circle, and red and black squares show the locations of the extremum points. (b) Bifurcation diagram of the 1D model (18) showing subcritical pitchfork bifurcation.

Therefore, from the foregoing analysis of the one-dimensional model and the potential function $V(\xi)$, it is seen that the change of shape of the graphs of the the potential function with the variation of the parameter r determines the nature of transition to convection. The potential function, although, is a highly simplified description of the system under consideration, yet, it is able to capture the transition phenomena quite satisfactorily. It is interesting to note here that the mode Z_{201} considered in the vertical vorticity is very important in capturing the subcritical behavior in the system. We did not get subcritical convection excluding this particular mode, even by considering a large number of modes in the low dimensional modeling. The contour plots of the Z_{201} mode on the $x - z$ plane shown in Fig. 8(a) clearly depicts the rotating tendency of the fluid on that plane for Ta = 120 and Pr = 0.1. To understand the role of the Z_{201} mode in inducing subcriticality in
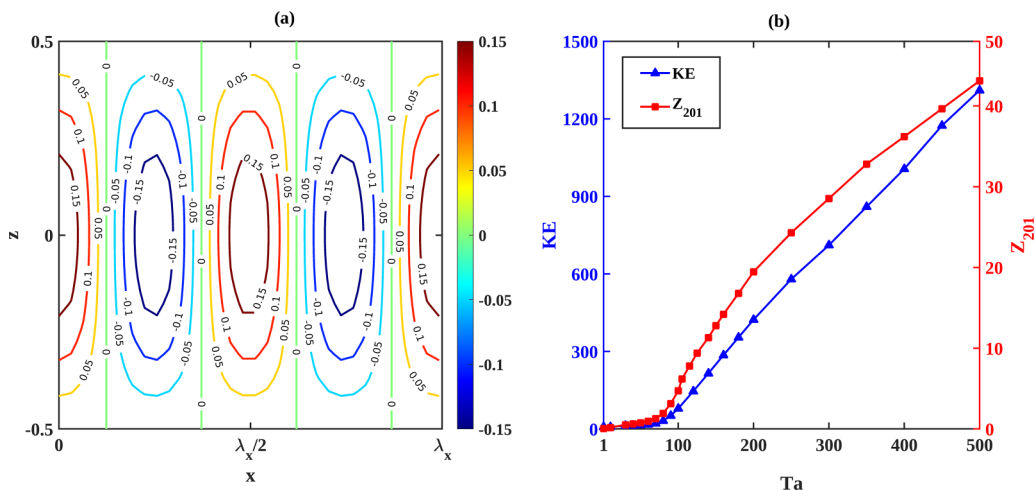

FIG. 8. (a) Contour plots of the vorticity mode Z_{201} showing the rotating tendency of the flow field on the $x - z$ plane as obtained from the 1D model (18) for Ta = 120 and Pr = 0.1. (b) Kinetic energy (KE) and the value of Z_{201} as a function of the Taylor number Ta for Pr = 0.1 at the onset of convection ($r = 1.001$) obtained from the five mode model (11)–(15). Vertical scales for the graphs of the KE and Z_{201} are shown along the left and right vertical axes, respectively.
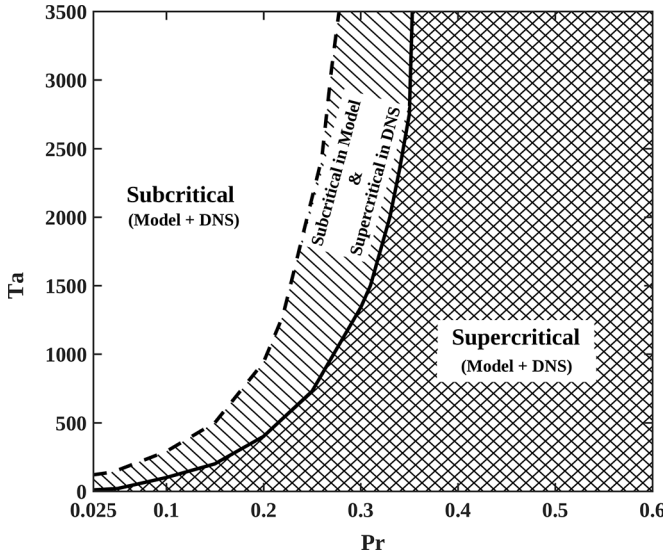
FIG. 9. Two parameter diagram constructed from the 1D model (18) and DNS for rigid boundary conditions demarcating supercritical and subcritical flow regimes on the $Pr - Ta$ plane. The thick solid and dashed black curves are obtained from the model and DNS, respectively.

the system, we compute the value of the Z_{201} mode and the kinetic energy (KE) from the five mode model (11)–(15) using the formula KE $= \frac{1}{2}\langle u_x^2 + u_y^2 + u_z^2 \rangle$, where $\langle \cdot \rangle$ denotes the space average over the domain $\frac{2\pi}{k_c} \times \frac{2\pi}{k_c} \times 1$.

The variation of Z_{201} and KE at the onset of convection ($r = 1.001$) with Ta are shown in Fig. 8(b) for $Pr = 0.1$. We note here that for $Pr = 0.1$, subcriticality is observed in the model when $Ta \geqslant 100$. Now from Fig. 8(b) it is clearly seen that the growth rate of the graph of Z_{201} greatly enhanced for $Ta \geqslant 100$. Simultaneously, the kinetic energy of the system also grows at a very fast rate with Ta at the onset of convection showing a clear correlation between the growth rate of Z_{201} and the kinetic energy. Now, very high kinetic energy at the onset of convection for $Ta \geqslant 100$, leads to the phenomenon of sustenance of convection in the subcritical regime ($r < 1$) during the backward continuation of the finite amplitude solution obtained at the onset. Thus, the mode Z_{201} plays a crucial role in inducing subcriticality in the system.

We now use the 1D model to demarcate the supercritical and subcritical onset of convection on the $Pr - Ta$ plane and results are shown in Fig. 9. It is clearly observed that increasing the rotation rate (Ta) promotes subcriticality, while increasing the Prandtl number (Pr) inhibits it by promoting supercriticality.

Now, to check the validity of the model results we perform three-dimensional direct numerical simulations of the system using the open source spectral element code NEK5000 [67] in a rectangular box of size $\frac{2\pi}{k_c} \times \frac{2\pi}{k_c} \times 1$ with grid resolution $56 \times 56 \times 56$. Time advancement is done by a suitable second order backward difference scheme with Courant-Friedrichs-Lewy (CFL) condition in the code. We use random initial conditions with time step $\delta t = 1 \times 10^{-4}$ for all the simulations. At the outset, we use the critical wave number k_c computed from the linear theory to restrict the computational domain to $\frac{2\pi}{k_c} \times \frac{2\pi}{k_c} \times 1$ and determine the critical Rayleigh number for the onset of convection. The results for $Pr = 0.1$ are presented in Table I which show a satisfactory match among the linear theory, model, and DNS.

In DNS, the subcritical and supercritical transitions to rotating convection are determined by computing the Nusselt number Nu, defined by

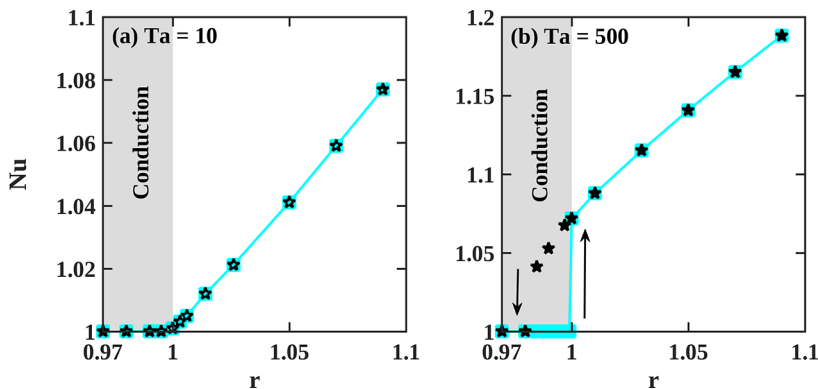$$Nu = 1 + Pr^2 \langle u_z \theta \rangle, \qquad (19)$$

FIG. 10. Variation of the Nusselt number Nu with r for Pr = 0.1. The solid cyan line and black stars, respectively, correspond to the forward and backward continuation data for (a) Ta = 10 and (b) Ta = 500.

which measures the ratio of the average convective to conductive heat transfers across the layers. The symbol $\langle \cdot \rangle$ represents the spatial average over the computational domain. Supercritical or subcritical convection occurs at the onset if the value of Nu follows the same or different paths during the forward and backward continuation of the reduced Rayleigh number across the critical point $r = 1$. Figure 10 shows the variations of the Nusselt numbers for Ta = 10 and 500. From Fig. 10(a), it is observed that for forward as well as backward continuation of r, the Nusselt number follows the same path and Nu does not show any jump at the critical point $r = 1$ indicating supercritical nature of the transition. On the other hand, Fig. 10(b) shows a discontinuity in Nu, and forward and backward data following different paths forming the so called "hysteresis loop" indicating the subcritical transition to convection. For a detailed understanding of the parameter space, we now determine the curve separating the supercritical and subcritical onset of the convection flow regime which is shown using the thick dashed black curve in Fig. 9. Thus, the model and the DNS results show qualitatively similar behavior. Subsequently, we investigate the phenomenon of subcritical convection in RRBC in the presence of free-slip boundary conditions.

2. Results for free-slip boundary conditions

It is interesting to note that subcritical convection was first reported in the RRBC model in the presence of free-slip boundary conditions [45,58] before the experimental observation of the phenomenon by Rossby [42]. Both weakly nonlinear theory [45] and low dimensional modeling [58] were used for the investigation. Following the low dimensional modeling approach presented in [58], we expand the convective vertical velocity, vorticity, and temperature fields as follows:

$$v_z = W_{101}(t) \cos k_c x \sin \pi z, \tag{20}$$

$$\omega_z = Z_{101}(t) \cos k_c x \cos \pi z + Z_{200} \cos 2k_c x, \tag{21}$$

$$\theta = T_{101}(t) \cos k_c x \sin \pi z + T_{002}(t) \sin 2\pi z, \tag{22}$$

in terms of the boundary condition compatible basis functions. We then project the hydrodynamic equations (1a)–(1c) on these modes to obtain a five-dimensional coupled ordinary differential

TABLE II. Critical Rayleigh numbers (Ra_c) for different Ta computed from linear theory (LT), 1D model, and DNS for $Pr = 0.1$ with free-slip boundary conditions.

Ta	k_c (LT)	Ra_c (LT)	Ra_c (Model)	Ra_c (DNS)	Error(%) (LT vs Model)	Error(%) (LT vs DNS)
1	2.226	659.5	659.5	660	0	0.07
10	2.269	677.1	677.1	675	0	0.31
50	2.434	748.3	748.3	720	0	3.78
100	2.594	826.2	826.2	775	0	6.19
500	3.277	1274.6	1274.5	1090	0.01	14.48

equation for the Fourier amplitudes W_{101}, Z_{101}, Z_{200}, T_{101}, and T_{002} which is given by

$$\dot{\xi} = -(a^2\xi - c\phi + b\gamma)/a, \tag{23}$$

$$\dot{\gamma} = -a\gamma + b\xi - \pi/2\chi\xi, \tag{24}$$

$$\dot{\chi} = -4k^2\chi + \pi\xi\gamma, \tag{25}$$

$$\dot{\phi} = -(a\phi - \xi - \pi Pr\xi\psi)/Pr, \tag{26}$$

$$\dot{\psi} = -\pi/2(8\pi\psi + Pr\xi\phi)/Pr, \tag{27}$$

where $\xi = W_{101}$, $\gamma = Z_{101}$, $\chi = Z_{200}$, $\phi = T_{101}$, $\psi = T_{002}$, $a = \pi^2 + k_c^2$, $b = \pi\sqrt{Ta}$, $c = Rak_c^2$.

As done with rigid boundary conditions, here also we compare the critical Rayleigh number for the onset of convection determined from the linear theory (LT) and the above model. The comparison results are presented in Table II which shows a very good match. We then further reduce the set of five ordinary differential equations to a single one by adopting a similar procedure as described in the previous subsection. Thus, we obtain the following one-dimensional model

$$\dot{\xi} = d_1\xi + d_3\xi^3 + d_5\xi^5, \tag{28}$$

for the investigation of subcritical bifurcation, where, $\xi = W_{101}$, $d_1 = 64a^4(a - \pi^2) + 64ab^2(a - \pi^2) - 64ac(a - \pi^2)$, $d_5 = \pi^2Pr^2a^2$, $d_3 = 8a^3Pr^2(a - \pi^2) + 8a^3\pi^2 + 8b^2Pr^2(a - \pi^2) - 8c\pi^2$.

Interestingly, even after the drastic simplification, the critical Rayleigh number for the onset of convection determined from the above 1D model is the same as the ones determined from the five mode model. We have also checked that the one-dimensional model (28) provides qualitatively the same bifurcation structure as the one given by the five mode model (23)–(27) in the stationary cellular convection regime. Therefore, we use the model (28) for the investigation of subcritical convection and the effect of the parameters on it. Figure 11 shows the regions of subcritical and supercritical onset of convection regimes on the $Pr - Ta$ plane obtained from the 1D model separated by the thick solid black curve. The region on the left of the solid curve is for subcritical convection, while the region on the right side of the curve is for supercritical convection.

For the validation, next, we perform direct numerical simulations of the system in the presence of free-slip boundary conditions using an open source pseudospectral code *Tarang* [68]. The simulations are performed in a domain of dimensions $2\pi/k_c \times 2\pi/k_c \times 1$ with 32^3 spatial grids (k_c is the critical wave number determined from the linear theory). In the code, the independent convective fields are expanded using the Fourier basis functions as

$$(u_z, \theta) = \sum_{l,m,n} (W_{lmn}(t), T_{lmn}(t))e^{i(lk_xx+mk_yy)} \sin(n\pi z), \tag{29}$$

$$(u_x, u_y) = \sum_{l,m,n} (U_{lmn}(t), V_{lmn}(t))e^{i(lk_xx+mk_yy)} \cos(n\pi z), \tag{30}$$
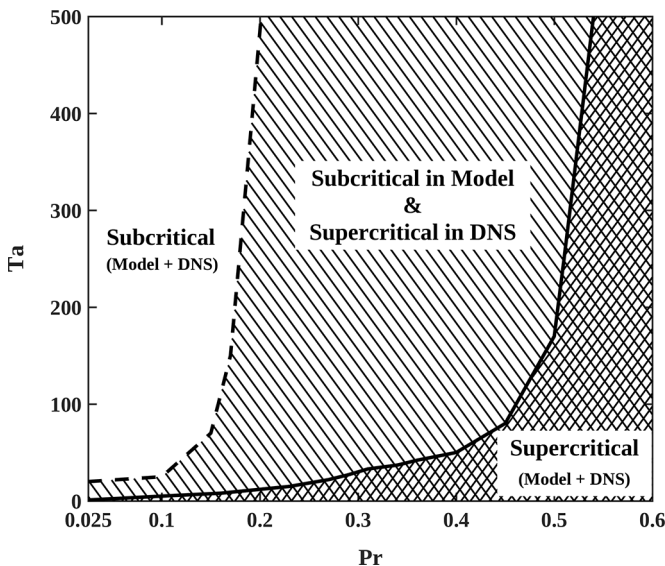
FIG. 11. Two parameter diagram computed from the 1D model and DNS for free-slip boundary conditions demarcating supercritical and subcritical flow regimes on the Pr − Ta plane. The thick solid and dashed black curves are obtained from the model and DNS, respectively.

where U_{lmn}, V_{lmn}, W_{lmn}, and T_{lmn} are the Fourier modes amplitudes with l, m, and n being the non-negative integers. k_x and k_y are the horizontal wave numbers along x and y directions, respectively, such that $k_c^2 = k_x^2 + k_y^2$. Time advancement is done using the fourth order Runge-Kutta (RK4) scheme with CFL condition considering maximum time step $\Delta t = 0.001$.

Using the above procedure, we perform extensive DNS of the system and determine the boundary delimiting the regions of supercritical and subcritical onset of convection on the Pr − Ta plane. Note that the subcritical and supercritical onset of convection are determined by computing the Nusselt number with the forward and backward variation of the Rayleigh number around the critical Rayleigh number for the onset of convection as was done for the rigid boundary conditions. The boundary is shown with a dashed black line in Fig. 11. The difference between the boundaries delimiting the subcritical and supercritical regions obtained from the model and DNS is more here compared to the rigid boundary case. The reason may be attributed to the drastic simplification of the system in terms of only five modes, while the DNS is performed on a grid of size $56 \times 56 \times 56$. Nonetheless, the flow patterns observed at the supercritical and subcritical regimes are similar both in model and DNS. It is clearly understood from the model that like rigid boundary conditions, the finite amplitude solutions observed at the onset of convection are of subcritical origin. Much like the rigid boundary conditions, the rotation rate in this case also appears to promote the subcritical convection, while the Prandtl number inhibits it. Thus, the change of boundary conditions does not bring qualitative change on the onset of convection.

B. Overstability

The five mode models (11)–(15) and (23)–(27) not only help to provide the simplest possible descriptions of the stationary supercritical and subcritical onset of rotating convection in terms of one-dimensional models (18) and (28), but also captures the phenomenon of overstable convection leading to small amplitude time dependent periodic solution near the onset of convection. In this section, we utilize the five mode models to investigate the onset of overstable convection. First, we use the critical wave number for the onset of overstable convection (k_o) obtained from linear theory both for rigid and free-slip boundary conditions and determine the critical Rayleigh number

TABLE III. Critical Rayleigh numbers (Ra_o) and wave number (k_o) at the onset of overstability computed from the linear theory (LT), 1D model, and DNS for rigid and free-slip boundary conditions.

Pr	Ta	k_o (LT)	Ra_o (LT)	Ra_o (Model)	Ra_c (DNS)	Error(%) (LT vs Model)	Error(%) (LT vs DNS)
0.1 (Rigid)	2×10^4	3.513	6418	5803	6360	9.59	0.90
	3×10^4	3.662	6978	6142	7000	11.98	0.31
	5×10^4	3.901	7938	6735	7955	15.15	0.21
0.025 (Rigid)	1×10^4	2.983	4365	4252	4370	3.14	0.11
	2×10^4	2.996	4507	4286	4518	4.90	0.24
	5×10^4	3.036	4812	4396	4860	8.64	0.99
0.1 (Free-slip)	1×10^3	2.261	1482	1484	1485	0.13	0.20
	5×10^3	2.401	1614	1615	1615	0.06	0.06
	1×10^4	2.543	1760	1762	1765	0.11	0.28
0.025 (Free-slip)	1×10^3	2.224	1350	1351	1352	0.07	0.14
	5×10^3	2.237	1360	1361	1362	0.07	0.14
	1×10^4	2.250	1372	1373	1375	0.07	0.21

for the onset of overstable convection (Ra_o) in the five-dimensional models and DNS. The list of values of Ra_o obtained from linear theory, five mode models, and DNS are presented in Table III and compared for two Prandtl numbers. It is interesting to note here that in the entire overstable regime determined from the linear theory (see Fig. 2), the five mode models as well as DNS exhibit periodic solution of overstable origin at the onset of convection.

Inspired by the above observation, we move ahead and construct bifurcation diagrams using both the five mode models for two different Prandtl numbers (Pr = 0.025, 0.1). We choose Ta = 2×10^4 for rigid boundary conditions, while for free-slip boundary conditions we take Ta = 10^3. The parameters are chosen in such a way that the oscillatory mode of convection of overstable origin is observed at the onset. The bifurcation diagrams presented in Figs. 12(a) and 12(b) clearly show the birth of a small amplitude oscillatory solution through supercritical Hopf bifurcation. The temporal evolution of the flow patterns corresponding to oscillatory solutions for rigid boundary conditions is shown in Fig. 12(c). The flow patterns corresponding to the oscillatory solutions of overstable origin for free-slip boundary conditions are also similar. We have checked that the flow patterns obtained from the DNS, both for rigid and free-slip boundary conditions, are also similar. Thus, the five-dimensional models qualitatively capture the overstable convection in the considered parameter regime.

V. CONCLUSIONS

In summary, we have investigated the transition to convection in rotating Rayleigh-Bénard convection with rigid and free-slip boundary conditions by performing low dimensional modeling and direct numerical simulations in the Prandtl number range $0 < \text{Pr} \leqslant 0.6$. The Taylor number is varied in the ranges $0 < \text{Ta} \leqslant 5 \times 10^4$ and $0 < \text{Ta} \leqslant 10^4$ for rigid and free-slip boundary conditions, respectively.

Extensive three-dimensional direct numerical simulations performed with both rigid and free-slip boundary conditions in the considered parameter regime reveal stationary as well as oscillatory flow patterns at the onset of convection which can be of subcritical and supercritical origin. The supercritical flow regime is characterized by the appearance of small amplitude two-dimensional rolls solutions at the onset. On the other hand, finite amplitude stationary two-dimensional flow patterns are manifested at the onset of subcritical convection. For the time dependent flow regime of overstable origin, small amplitude oscillatory solutions are observed at the onset.
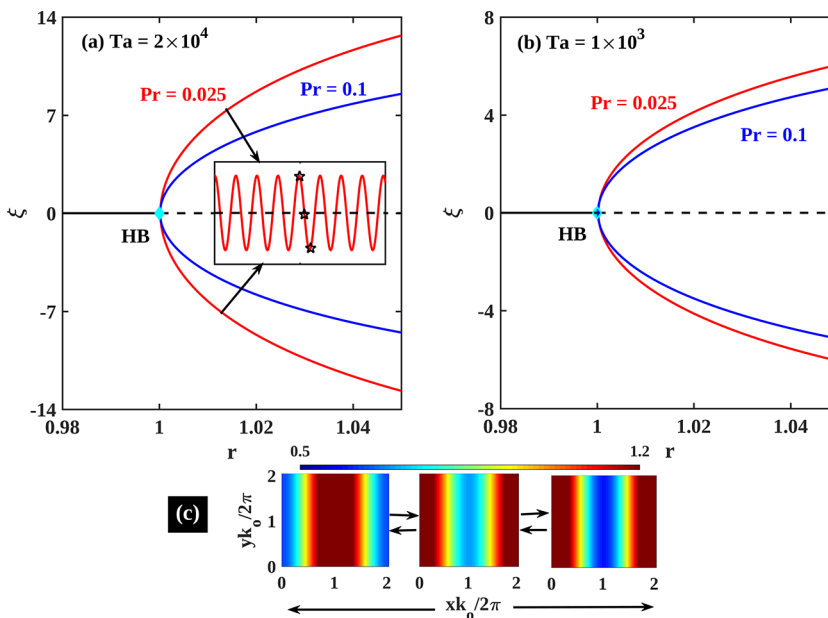
FIG. 12. Bifurcation diagrams constructed from the 5D models for two Pr values by plotting the extremum values of the variable ξ corresponding to different solutions with the variation of r. Stable and unstable solutions are represented by solid and dashed lines, respectively. The cyan filled diamond at $r = 1$ indicates the supercritical Hopf bifurcation (HB) point. The solid black curve represents the conduction state, while the red and blue curves correspond to the stable limit cycles. In (a) and (b) rigid and free-slip boundary conditions are considered, respectively. The inset in (a) displays the time evolution of ξ corresponding to the limit cycle solutions for Pr = 0.025. (c) Isotherms computed at the mid plane corresponding to the marked points in the inset of (a).

For the simplified mathematical description of the above observations, we perform low dimensional modeling of the system. To our surprise, this led to the simplest possible description of the stationary supercritical and subcritical rotating convection in terms of a one-dimensional model both for rigid and free-slip boundary conditions. The bifurcation analysis of the one-dimensional models shows that the supercritical and subcritical flow regimes are associated with the pitchfork bifurcations of a similar type. The models are then used to identify different stationary flow regimes on the $Pr - Ta$ plane and compared with the ones obtained from the DNS. Both the 1D models for rigid and free-slip boundary conditions show a qualitative match with the DNS results, despite drastic simplification. Interestingly, a better match is observed with the DNS results for the model with rigid boundary conditions. Here we note that, despite the qualitative match, the simple models get the locations of the subcritical bifurcation points fairly significantly off from that of the DNS. This deviation is solely due to the severe truncation in the expansions of the independent fields considered for low dimensional modeling. For a better match with the results of DNS which are performed with $32 \times 32 \times 32$ and $56 \times 56 \times 56$ grid resolutions for free-slip and rigid boundary conditions, respectively, one needs to consider more modes in the low dimensional modeling. However, our focus in this work has been to capture the transitions qualitatively using the simplest possible equations. The simultaneous analysis of the low dimensional models and DNS data show that irrespective of the boundary conditions, the finite amplitude solution associated with the subcritical pitchfork bifurcation, is dominantly observed for low Prandtl number fluids in the considered range of the Taylor number in this paper. The Taylor number is observed to encourage subcritical behavior as it is increased, whereas, the increasing Prandtl number suppresses it. This observation is consistent with the results of the previous numerical simulations [22,59].

Further, we also derive two five-dimensional models to study the overstable onset of convection in the presence of rigid and free-slip boundaries. The models nicely explain the origin of small amplitude time dependent flow patterns in the region of overstable convection determined from the linear theory. The results presented in the paper show that despite the very high complexity of the RRBC system, the effective dynamics of the system close to the onset can be captured by a very simple set of ordinary differential equations. We expect that similar analysis will be helpful to gain insight into the dynamics of different complex systems including thermal convection in the simultaneous presence of rotation and external magnetic field.

[1] G. A. Glatzmaier, R. S. Coe, L. Hongre, and P. H. Roberts, The role of the earth's mantle in controlling the frequency of geomagnetic reversals, Nature (London) **401**, 885 (1999).

[2] E. Knobloch, N. O. Weiss, and L. N. Da Costa, Oscillatory and steady convection in a magnetic field, J. Fluid Mech. **113**, 153 (1981).

[3] P. A. Davidson, Magnetohydrodynamics in materials processing, Annu. Rev. Fluid Mech. **31**, 273 (1999).

[4] S. Chandrasekhar, *Hydrodynamic and Hydromagnetic Stability* (Cambridge University Press, Cambridge, 1961).

[5] M. K. Verma, *Physics of Buoyant Flows: From Instabilities to Turbulence* (World Scientific, Singapore, 2018).

[6] J. B. Elliott, L. G. Moretto, L. Phair, G. J. Wozniak, L. Beaulieu, H. Breuer, R. G. Korteling, K. Kwiatkowski, T. Lefort, L. Pienkowski, Liquid to vapor phase transition in excited nuclei, Phys. Rev. Lett. **88**, 042701 (2002).

[7] G. Ahlers, S. Grossmann, and D. Lohse, Heat transfer and large scale dynamics in turbulent Rayleigh-Bénard convection, Rev. Mod. Phys. **81**, 503 (2009).

[8] H. Xie, F. Yin, T. Yu, J.-T. Wang, and C. Liang, Mechanism for direct graphite-to-diamond phase transition, Sci. Rep. **4**, 5930 (2014).

[9] S. Eich, M. Plötzing, M. Rollinger, S. Emmerich, R. Adam, C. Chen, H. C. Kapteyn, M. M. Murnane, L. Plucinski, D. Steil, Band structure evolution during the ultrafast ferromagnetic-paramagnetic phase transition in cobalt, Sci. Adv. **3**, e1602094 (2017).

[10] J. Marshall and F. Schott, Open-ocean convection: Observations, theory, and models, Rev. Geophys. **37**, 1 (1999).

[11] I. R. Kirillov, C. B. Reed, L. Barleon, and K. Miyazaki, Present understanding of mhd and heat transfer phenomena for liquid metal blankets, Fusion Eng. Des. **27**, 553 (1995).

[12] J. M. Aurnou and P. L. Olson, Experiments on Rayleigh–Bénard convection, magnetoconvection and rotating magnetoconvection in liquid gallium, J. Fluid Mech. **430**, 283 (2001).

[13] E. J. Kaplan, N. Schaeffer, J. Vidal, and P. Cardin, Subcritical thermal convection of liquid metals in a rapidly rotating sphere, Phys. Rev. Lett. **119**, 094501 (2017).

[14] D. T. J. Hurle, Hydrodynamics, convection and crystal growth, J. Cryst. Growth **13-14**, 39 (1972).

[15] B. I. Halperin, T. C. Lubensky, and S. K. Ma, First-order phase transitions in superconductors and smectic-a liquid crystals, Phys. Rev. Lett. **32**, 292 (1974).

[16] E. Bodenschatz, W. Pesch, and G. Ahlers, Recent developments in Rayleigh-Bénard convection, Annu. Rev. Fluid Mech. **32**, 709 (2000).

[17] M. Net, F. Garcia, and J. Sánchez, On the onset of low-Prandtl-number convection in rotating spherical shells: non-slip boundary conditions, J. Fluid Mech. **601**, 317 (2008).

[18] M. K. Verma, A. Kumar, and A. Pandey, Phenomenology of buoyancy-driven turbulence: Recent results, New J. Phys. **19**, 025012 (2017).

[19] Y. Nandukumar, S. Chakraborty, M. K. Verma, and R. Lakkaraju, On heat transport and energy partition in thermal convection with mixed boundary conditions, Phys. Fluids **31**, 066601 (2019).

[20] R. G. Cooper, P. J. Bushby, and C. Guervilly, Subcritical dynamos in rapidly rotating planar convection, Phys. Rev. Fluids **5**, 113702 (2020).

[21] M. Ghosh, P. Ghosh, Y. Nandukumar, and P. Pal, Transitions near the onset of low Prandtl-number rotating convection in presence of horizontal magnetic field, Phys. Fluids **32**, 024110 (2020).

[22] S. Mandal, M. Ghosh, P. Maity, A. Banerjee, and P. Pal, Supercritical and subcritical rotating convection in a horizontally periodic box with no-slip walls at the top and bottom, Phys. Fluids **34**, 104117 (2022).

[23] S. Mandal, S. Sarkar, and P. Pal, Effect of horizontal magnetic field on Küppers–Lortz instability, Phys. Fluids **35**, 074118 (2023).

[24] F. H. Busse and J. A. Whitehead, Instabilities of convection rolls in a high Prandtl number fluid, J. Fluid Mech. **47**, 305 (1971).

[25] R. M. Clever and F. H. Busse, Convection at very low Prandtl numbers, Phys. Fluids A **2**, 334 (1990).

[26] H. K. Pharasi and K. Kumar, Oscillatory instability and fluid patterns in low-Prandtl-number Rayleigh-Bénard convection with uniform rotation, Phys. Fluids **25**, 104105 (2013).

[27] S. Dan, P. Pal, and K. Kumar, Low-Prandtl-number Rayleigh-Bénard convection with stress-free boundaries, Eur. Phys. J. B **87**, 278 (2014).

[28] M. C. Cross and P. C. Hohenberg, Pattern formation outside of equilibrium, Rev. Mod. Phys. **65**, 851 (1993).

[29] R. Hoyle and R. B. Hoyle, *Pattern Formation: An Introduction to Methods* (Cambridge University Press, 2006).

[30] P. Pal, K. Kumar, P. Maity, and S. K. Dana, Pattern dynamics near inverse homoclinic bifurcation in fluids, Phys. Rev. E **87**, 023001 (2013).

[31] E. Knobloch, D. R. Moore, J. Toomre, and N. O. Weiss, Transitions to chaos in two-dimensional double-diffusive convection, J. Fluid Mech. **166**, 409 (1986).

[32] S. Paul, P. Wahi, and M. K. Verma, Bifurcations and chaos in large-Prandtl number Rayleigh–Bénard convection, Int. J. Non Linear Mech. **46**, 772 (2011).

[33] Y. Nandukumar and P. Pal, Oscillatory instability and routes to chaos in Rayleigh-Bénard convection: Effect of external magnetic field, Europhys. Lett. **112**, 24003 (2015).

[34] C. Rumford, Of the propagation of heat in fluids, *Complete Works* (American Academy of Arts and Sciences, Boston, 1870) , Vol. 1, p. 239.

[35] O. Thual, Zero-Prandtl-number convection, J. Fluid Mech. **240**, 229 (1992).

[36] P. Manneville, *Instabilities, Chaos and Turbulence*, Vol. 1 (World Scientific, 2010).

[37] R. E. Ecke and O. Shishkina, Turbulent rotating Rayleigh-Bénard convection, Annu. Rev. Fluid Mech. **55**, 603 (2023).

[38] S. H. Strogatz, *Nonlinear Dynamics And Chaos: With Applications To Physics, Biology, Chemistry, And Engineering* (Westview Press, 2001).

[39] M. Evonuk and G. A. Glatzmaier, The effects of rotation rate on deep convection in giant planets with small solid cores, Planet. Space Sci. **55**, 407 (2007).

[40] N. J. Wickett, S. Mirarab, N. Nguyen, T. Warnow, E. Carpenter, N. Matasci, S. Ayyampalayam, M. S. Barker, J. G. Burleigh, M. A. Gitzendanner, Phylotranscriptomic analysis of the origin and early diversification of land plants, Proc. Natl. Acad. Sci. USA **111**, E4859 (2014).

[41] M. S. Miesch, The coupling of solar convection and rotation (invited review), in *Helioseismic Diagnostics of Solar Convection and Activity* (Springer, 2000), pages 59–89.

[42] H. T. Rossby, A study of Bénard convection with and without rotation, J. Fluid Mech. **36**, 309 (1969).

[43] Y. Nakagawa, An experiment on the inhibition of thermal convection by a magnetic field, Nature (London) **175**, 417 (1955).

[44] D. Fultz and Y. Nakagawa, Experiments on over-stable thermal convection in mercury, Proc. R. Soc. London, Ser. A **231**, 211 (1955).

[45] G. Veronis, Cellular convection with finite amplitude in a rotating fluid, J. Fluid Mech. **5**, 401 (1959).

[46] I. A. Eltayeb, Hydromagnetic convection in a rapidly rotating fluid layer, Proc. R. Soc. London A **326**, 229 (1972).

[47] T. Clune and E. Knobloch, Pattern selection in rotating convection with experimental boundary conditions, Phys. Rev. E **47**, 2536 (1993).

[48] K. Julien and E. Knobloch, Fully nonlinear three-dimensional convection in a rapidly rotating layer, Phys. Fluids **11**, 1469 (1999).

[49] K. Julien, S. Legg, J. McWilliams, and J. Werne, Rapidly rotating turbulent Rayleigh-Bénard convection, J. Fluid Mech. **322**, 243 (1996).

[50] R. P. J. Kunnen, H. J. H. Clercx, and B. J. Geurts, Heat flux intensification by vortical flow localization in rotating convection, Phys. Rev. E **74**, 056306 (2006).

[51] I. Grooms, K. Julien, J. B. Weiss, and E. Knobloch, Model of convective taylor columns in rotating Rayleigh-Bénard convection, Phys. Rev. Lett. **104**, 224501 (2010).

[52] P. Maity, K. Kumar, and P. Pal, Homoclinic bifurcations in low-Prandtl-number Rayleigh-Bénard convection with uniform rotation, Europhys. Lett. **103**, 64003 (2013).

[53] P. Maity and K. Kumar, Zero-Prandtl-number convection with slow rotation, Phys. Fluids **26**, 104103 (2014).

[54] S. Sakai, The horizontal scale of rotating convection in the geostrophic regime, J. Fluid Mech. **333**, 85 (1997).

[55] P. Vorobieff and R. E. Ecke, Turbulent rotating convection: An experimental study, J. Fluid Mech. **458**, 191 (2002).

[56] K. M. Bajaj, G. Ahlers, and W. Pesch, Rayleigh-Bénard convection with rotation at small Prandtl numbers, Phys. Rev. E **65**, 056309 (2002).

[57] G. M. Vasil, K. Julien, and N. A. Featherstone, Rotation suppresses giant-scale solar convection, Proc. Natl. Acad. Sci. USA **118**, 1 (2021).

[58] G. Veronis, Motions at subcritical values of the Rayleigh number in a rotating fluid, J. Fluid Mech. **24**, 545 (1966).

[59] R. M. Clever and F. H. Busse, Nonlinear properties of convection rolls in a horizontal layer rotating about a vertical axis, J. Fluid Mech. **94**, 609 (1979).

[60] A. Oberbeck, Ueber die Wärmeleitung der Flüssigkeiten bei Berücksichtigung der Strömungen infolge von Temperaturdifferenzen, Ann. Phys. Chem. **243**, 271 (1879).

[61] J. Boussinesq, *Théorie Analytique de la Chaleur*, Vol. 2 (Gauthier-Villars, 1903).

[62] M. R. Khorrami, M. R. Malik, and R. L. Ash, Application of spectral collocation techniques to the stability of swirling flows, J. Comput. Phys. **81**, 206 (1989).

[63] L. Kaufman, Some thoughts on the QZ algorithm for solving the generalized eigenvalue problem, ACM Trans. Math. Software **3**, 65 (1977).

[64] P. Glendinning, J. Abshagen, and T. Mullin, Imperfect homoclinic bifurcations, Phys. Rev. E **64**, 036208 (2001).

[65] M. K. Verma and R. K. Yadav, Supercriticality to subcriticality in dynamo transitions, Phys. Plasmas **20**, 1 (2013).

[66] B. Ermentrout, *Simulating, Analyzing, and Animating Dynamical Systems: A Guide to XPPAUT for Researchers and Students* (SIAM, 2002).

[67] P. F. Fischer, J. W. Lottes, and S. G. Kerkemeier, nek5000 web page, 2008.

[68] M. K. Verma, A. Chatterjee, K. S. Reddy, R. K. Yadav, S. Paul, M. Chandra, and R. Samtaney, Benchmarking and scaling studies of pseudospectral code tarang for turbulence simulations, Pramana **81**, 617 (2013).